nature electronics

ARTICLES

https://doi.org/10.1038/s41928-021-00622-9

Check for updates

Direct ink writing of three-dimensional thermoelectric microarchitectures

Fredrick Kim[1,5], Seong Eun Yang[1,5], Hyejin Ju[1,5], Seungjun Choo[1], Jungsoo Lee[1], Gyeonghun Kim[2], Soo-ho Jung[3], Suntae Kim[1], Chaenyung Cha[1], Kyung Tae Kim[3], Sangjoon Ahn[2], Han Gi Chae[1]✉ and Jae Sung Son[1,4]✉

Microthermoelectric modules can be used as energy harvesters, active coolers and thermal sensors in integrated systems. However, manufacturing such modules with traditional microfabrication processes is costly and produces only two-dimensional thermoelectric films, which limit the formation of high-temperature gradients and thus the amount of power generated. Here we show that microscale three-dimensional thermoelectric architectures can be fabricated through the direct writing of particle-based thermoelectric inks. Using size control and surface oxidation, the characteristics of $(Bi,Sb)_2(Te,Se)_3$-based particle inks are engineered to create colloidal inks with high viscoelasticity and without organic binders, and the inks are directly written into complex architectures using a 3D printing process. The resulting structures exhibit high thermoelectric figures of merit of 1.0 (p type) and 0.5 (n type), which are comparable to those of bulk ingots. Microthermoelectric generators made from three-dimensionally written vertical filaments exhibit large temperature gradients and a power density of 479.0 μW cm^{-2}.

Microthermoelectric modules (μTEMs) can be used to generate power from minimal heat flow or act as coolers for local heat management[1,2]. Depending on the dimensions of the thermoelectric (TE) legs, μTEMs can be integrated into various emerging systems—including the Internet of Things, wearables, wireless sensor networks and lab-on-a-chip devices[3–5]: many of these are expected to be energy-autonomous systems as they are embedded in enclosed environments or packaged within inaccessible structures[5–7]. Simple device structure, high reliability and durability, and maintenance-free operation of μTEMs makes them a promising solution for ensuring sustainable electricity supply for autonomous integrated systems. Arrays of μTEMs can also be potentially used in sensing applications such as high-resolution infrared image sensors, gas sensors and thermal imaging sensors[8].

The design and fabrication of microscale integrated systems that contain multiple functional electrical and mechanical components have been facilitated by developments in microelectromechanical systems (MEMS)[9]. MEMS microfabrication processes—which are based on traditional lithography, deposition, etching and release—can provide patterned, planar two-dimensional (2D) TE legs and electrodes in μTEMs with thicknesses in the range of tens of micrometres[10,11]. However, mass fabrication techniques used in MEMS are potentially costly, relying on complicated multistep processes and requiring expensive lithography equipment. Furthermore, 2D design processes are not suitable for the fabrication of three-dimensional (3D) TE legs with high aspect ratios in a μTEM. Such 3D structures are especially critical for creating a large temperature gradient across a TE leg and obtaining high power in a microthermoelectric generator (μTEG)[12,13]. Bulk micromachining has been used to fabricate 3D structures, but the approach is limited in terms of materials, scale and complexity, and it involves high cost and long processing time[9,14].

3D printing can be used to manufacture complex 3D structures[15,16]. Materials that can be printed on a micrometre or nanometre scale are, however, still mostly limited to photo-curable resins or their composites with inorganics, and printing is carried out by stereolithographic techniques[17]. Alternatively, colloidal inks containing inorganic particles or precursors can be printed using extrusion-based direct writing processes that offer processing simplicity and use affordable equipment, and are compatible with a wide range of printable materials[18,19]. In direct ink writing, it is important to optimize the viscoelastic properties of functional inks to a highly specific range, to maintain structural integrity during printing and functionality of the printed object[20,21]. Adding organic binders—the typical method to secure viscoelasticity—often leads to the critical degradation of electrical or mechanical functionality of inorganic printed objects, especially TE materials, due to lowered sintering efficiency[22–25]. Several approaches have been reported to fabricate Bi_2Te_3, BiSbTe, SnSe and skutterudites-based TE materials and modules by various 3D printing processes[22–27]. For example, inorganic ionic binders have been used to achieve moderate viscoelasticity in colloidal inks and perform layer-wise deposition of 3D TE structures without degradation of TE performance[28,29]. However, 3D-printed TE structures have low resolution due to the limited printability of inks and diminished functionality of printed materials.

In this Article, we report the development of high-viscoelasticity $(Bi,Sb)_2(Te,Se)_3$-based p- and n-type inks and show that they can be used for direct 3D writing. $(Bi,Sb)_2(Te,Se)_3$-based alloys are regarded as the most suitable TE materials for temperatures below 100 °C, making them candidates for power generation from low-grade

[1]Department of Materials Science and Engineering, Ulsan National Institute of Science and Technology (UNIST), Ulsan, Republic of Korea. [2]Department of Nuclear Engineering, Ulsan National Institute of Science and Technology (UNIST), Ulsan, Republic of Korea. [3]Department for 3D Printing Materials, Korea Institute of Materials Science (KIMS), Gyeongnam, Republic of Korea. [4]Center for Future Semiconductor Technology (FUST), Ulsan National Institute of Science and Technology (UNIST), Ulsan, Republic of Korea. [5]These authors contributed equally: Fredrick Kim, Seong Eun Yang, Hyejin Ju. ✉e-mail: hgchae@unist.ac.kr; jsson@unist.ac.kr

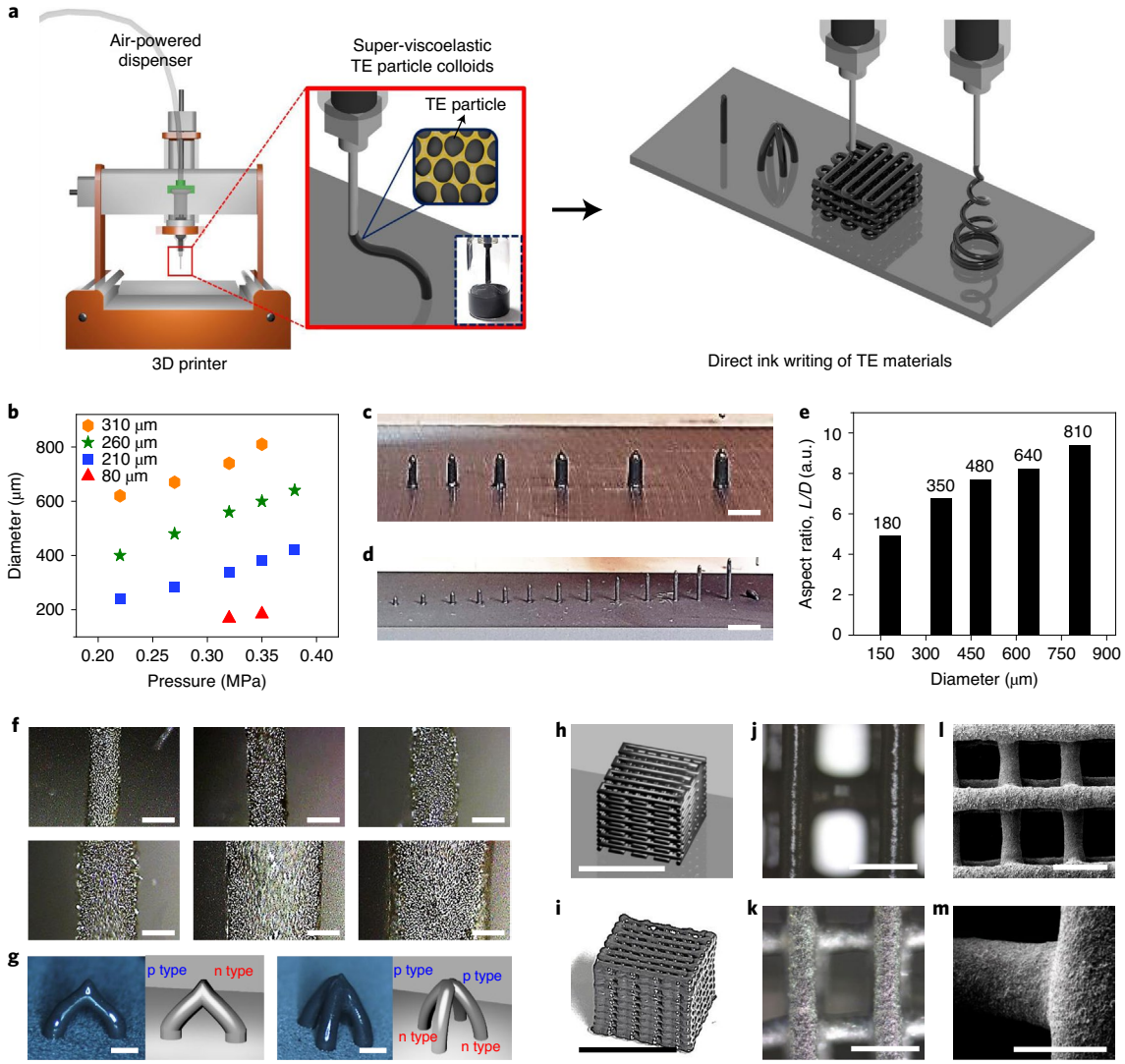

Fig. 1 | Direct 3D writing of TE inks. a, Schematic of the direct ink writing for 3D TE architectures. **b**, Plot of the diameters of 3D filaments versus the dispensing pressure with different inner diameters of nozzles. **c**,**d**, Photographs showing 3D filaments with different diameters (**c**) and aspect ratios (**d**). Scale bars, 2 mm. **e**, Maximum aspect ratio (length (*L*)/diameter (*D*)) of the written TE filaments with respect to the diameters. **f**, OM images of TE filaments with diameters of 180, 240, 340, 420, 560 and 620 μm. Scale bars, 200 μm. **g**, Charge-coupled device (CCD) images and illustrated premodels of arch-type architectures consisting of junctional p- and n-type TE legs. Scale bars, 500 μm. **h**,**i**, Illustrated model (**h**) and photograph (**i**) of a 3D lattice built by the layer-by-layer deposition of TE filaments. Scale bars, 10 mm. **j**,**k**, OM images of the as-printed (**j**) and sintered (**k**) 3D lattice. Scale bars, 500 μm. **l**,**m**, Low-magnification (**l**) and high-magnification (**m**) SEM images of the 3D lattice. Scale bars, 500 μm.

heat dissipated by integrated systems[30–34]. By manipulating various characteristics of TE particles (including size, size distribution and surface charge states), we create TE inks with high viscoelasticity and without using organic rheological modifiers. Direct 3D writing of inks is then used to print 3D filaments with high aspect ratios in a dimension-controlled manner, creating high-performance 3D TE architectures, including arches and lattices, via computer-aided design (CAD)-based design (Fig. 1a). To illustrate the capabilities of the direct writing process, we fabricate μTEGs and chip them with TE legs directly written on a substrate. Due to the high anisotropy of TE legs, the generators exhibit an output power of 2.8 μW at a temperature difference of 82.9 °C and a maximum power density of 479.0 μW cm^{-2}.

Three-dimensional direct ink writing of TE materials

The system used for the extrusion-based 3D direct ink writing of TE materials (Fig. 1a) consists of a nozzle connected to a syringe containing a viscoelastic TE ink, which is extruded by a pneumatic pressure controller that is moved in the *x*, *y* and *z* axes according to a CAD-based predesign. Considering the rheological properties of inks and the TE properties of sintered materials, p-type $Bi_{0.55}Sb_{1.45}Te_3$ with $Sb_2Te_4^{2-}$-based chalcogenidometallate (ChaM) content of 25 wt% and n-type $Bi_2Te_{2.7}Se_{0.3}$ with ChaM content of 10 wt% were chosen for the 3D printing experiments. The rheological and TE properties are discussed in the following sections. Standing TE filaments were vertically printed on a Si/SiO_2 substrate (Supplementary Video 1). The filaments exhibited excellent structural retention with smooth lateral surfaces in a single pass. Moreover, various printing parameters such as dispensing pressure and nozzle diameter were controlled, and therefore, the diameters of TE filaments were precisely controlled from 180 to 810 μm at the sintered states (Fig. 1b,c). This shows the applicability of the current process in multiple scales ranging from micrometres to millimetres. Optical microscopy (OM) images (Fig. 1f) showed that the written filaments

with various diameters had uniform linewidths with a standard deviation of less than 10 μm (Supplementary Fig. 1). The maximum aspect ratios achieved by the written filaments reached 4.9–9.4, depending on the diameter (Fig. 1d,e). This capability to print highly anisotropic 3D TE filaments by direct writing made it possible to build complex 3D architectures. As an example, Fig. 1g presents an arch-type architecture consisting of junctional p- and n-type TE legs fabricated by the direct writing process, where the uniformity in linewidth is not substantially changed at bent filaments or junctions. In addition, a 3D lattice was built by the layer-by-layer deposition of TE filaments (Fig. 1h,i and Supplementary Video 2). At the junctions, individual filaments maintained their primary architectures without merging or thickening, which demonstrates the structural retention of inks (Fig. 1j). These examples of complex 3D structures indicate the potential of using the proposed process to fabricate p–n junctions in 3D-patterned TE semiconductors and 3D porous TE structures for controlled thermal transport.

When the as-printed structures were heat treated, the TE particles in the 3D structures were well consolidated by the sintering promotion effect of the ChaM additives, leading to the formation of effectively sintered grains in the microstructure and robust 3D structures at the macroscale[28]. The OM and scanning electron microscopy (SEM) images of the sintered filaments in the printed 3D lattice (Fig. 1k,l) revealed that the TE filaments maintained their primary architecture. Moreover, the TE filaments at the junction were well fused together without crack formation (Fig. 1m). The high-resolution SEM images of p- and n-type TE filaments (Supplementary Fig. 2) show grain sizes of several tenths of a micrometre, which further indicated that grain growth was effective. Although large volume shrinkage is unavoidable in 3D-printed structures, high reproducibility was obtained for all the samples in all directions. Typically, the volume contracted by 36% during sintering at 450 °C for 30 min; these sintering conditions are required to obtain a competitive TE performance of materials. Thus, we could design the final 3D architecture according to the CAD-based predesign.

Ink design and rheological properties

Controlling the viscoelastic properties of inks is important for ensuring a reliable flow through fine nozzles and ensuring the structural integrity of the printed filament. Our group previously demonstrated that the addition of inorganic ChaM ions imparts the required viscoelasticity to TE-particle-containing colloidal inks, thereby facilitating the shape-conformable 3D printing of TE materials by layer-wise ink deposition[28]. However, the direct writing of TE inks without organic binders requires considerable improvement in the rheological properties to achieve smooth and reliable extrusion and faster structural recovery after printing. One way to enhance the viscosity is to increase the particle concentration, but this can also cause the nozzle clogging phenomenon. Therefore, obtaining high enough phase stability with high viscosity at a low particle concentration is the key to guarantee high-resolution 3D printing. Hence, we optimally design ink viscoelasticity by controlling the size, size distribution and surface states of the TE particles in the semidiluted regime of the volume fraction of particles (18.9 vol%). Figure 2a shows a schematic of the strategy used in the current study: controlling the TE particle size and size distribution as well as the surface oxidation of particles to obtain a stable ink system using ChaM.

Figure 2b,c and Supplementary Fig. 3 show the particle size distribution with a median particle size and the effect of distribution on the dynamic viscosities (η') of the corresponding TE particle colloids, respectively. A smaller average particle size and narrower particle size distribution produced higher η' in inks because the effective volume of a smaller particle system was greater. A wider distribution in the particle size may lead to aggregation, which can result in clogging during printing[35–39]. Accordingly, the shear stress dependencies of the storage (G') and loss (G'') moduli of colloidal inks (Supplementary Fig. 4) were measured to evaluate the linear viscoelasticity region and phase stability, respectively. The smallest TE particle system (D_{median} = 4.378 μm) exhibited higher critical stress value (30.8 Pa) than larger particle systems (for D_{median} of 8.759 and 17.276 μm, stress values were 4.2 and 1.5 Pa, respectively), indicating the ability to sustain higher shear stress without losing the structural integrity of the ink. In addition, higher G'' after critical stress may also suggest that the former system possesses superior phase stability compared with the latter cases[40]. It should be noted that regardless of the particle size, all the colloidal inks demonstrated higher G' than G'' in a wide range of shear stress values, indicating their highly viscous semisolid behaviour (Supplementary Fig. 4).

Our previous research showed that the addition of ChaM is necessary for obtaining high-quality TE devices by sintering, where voids are filled and the particles are structurally transformed from molecular ions to the crystalline phase[28]. Here we found that as-synthesized non-oxidized TE particles have weak negative surface charges (Fig. 2d). The inks composed of these non-oxidized TE particles are inherently unstable even in the presence of counterions of ethylenediammonium in the ChaM anions, which may screen the electrostatic surface charge on the TE particles ('screening effect') and induce irreversible aggregation[41]. To overcome this problem, controlled surface oxidation and the incorporation of ChaM were carried out to investigate their effect on the viscoelasticities of various inks. The degree of oxidation of the TE particles was investigated by zeta (ζ) potential measurement, Fourier transform infrared (FTIR) spectroscopy and X-ray photoelectron spectroscopy (XPS) (Fig. 2d,e and Supplementary Figs. 5 and 6). In both p- and n-type particles, X-ray diffraction (XRD) patterns of the oxidized particles were identical to those of the non-oxidized ones, suggesting that the oxidized surface layers were very thin or amorphic (Supplementary Fig. 7). However, the FTIR spectra of the oxidized particles clearly showed a peak indexed to OH stretching, which indicated surface oxidation; this observation was further supported by the XPS spectra, which showed oxide peaks. More importantly, the surface charges of TE particles became neutral by oxidation, minimizing the screening effect caused by the ChaM additives (Fig. 2d). Consequently, viscoelastic properties of the oxidized TE particles containing ChaM showed dramatic enhancement in various rheological properties, whereas those of the non-oxidized TE particles containing ChaM worsened owing to the screening effect. The quality of ChaM-containing inks was assessed by the rheological properties: shear stress dependency of G' (Fig. 2f and Supplementary Figs. 8–11), dynamic viscosity in the static state (Fig. 2g and Supplementary Figs. 8–11), initial slope of the increase in G' as a function of shear rate (Fig. 2h, top) and finally by the yield stress (Fig. 2h, bottom). It was clearly observed that ink with the smallest and largest non-oxidized particles was negatively affected by ChaM incorporation, but the oxidized-particle-based ink showed improvement in η' (Supplementary Figs. 8 and 10). However, the extent of improvement was not high enough compared with those having the smallest particles. Therefore, it was determined to use the smallest-particle-based TE ink. Also, the η' value of this direct-writable ink was two orders of magnitude higher than that of the 3D-printable ink in our previous study without an increase in volume fraction[28]. In addition, the structure recovery of inks after deposition is one of the most critical factors to ensure shape retention. To evaluate structure recovery, three interval thixotropy tests (3ITTs) were performed for comparing oxidized- and non-oxidized-particle-based inks with 25 wt% ChaM content (Fig. 2i). The 3ITTs are designed to measure the rate and degree of elastic recovery (G') after inducing structural disruption by increasing the shear stress. It is very important to note that the ink based on the oxidized TE particle exhibited reduced structure disruption on high shear stress and immediate elastic recovery compared with the

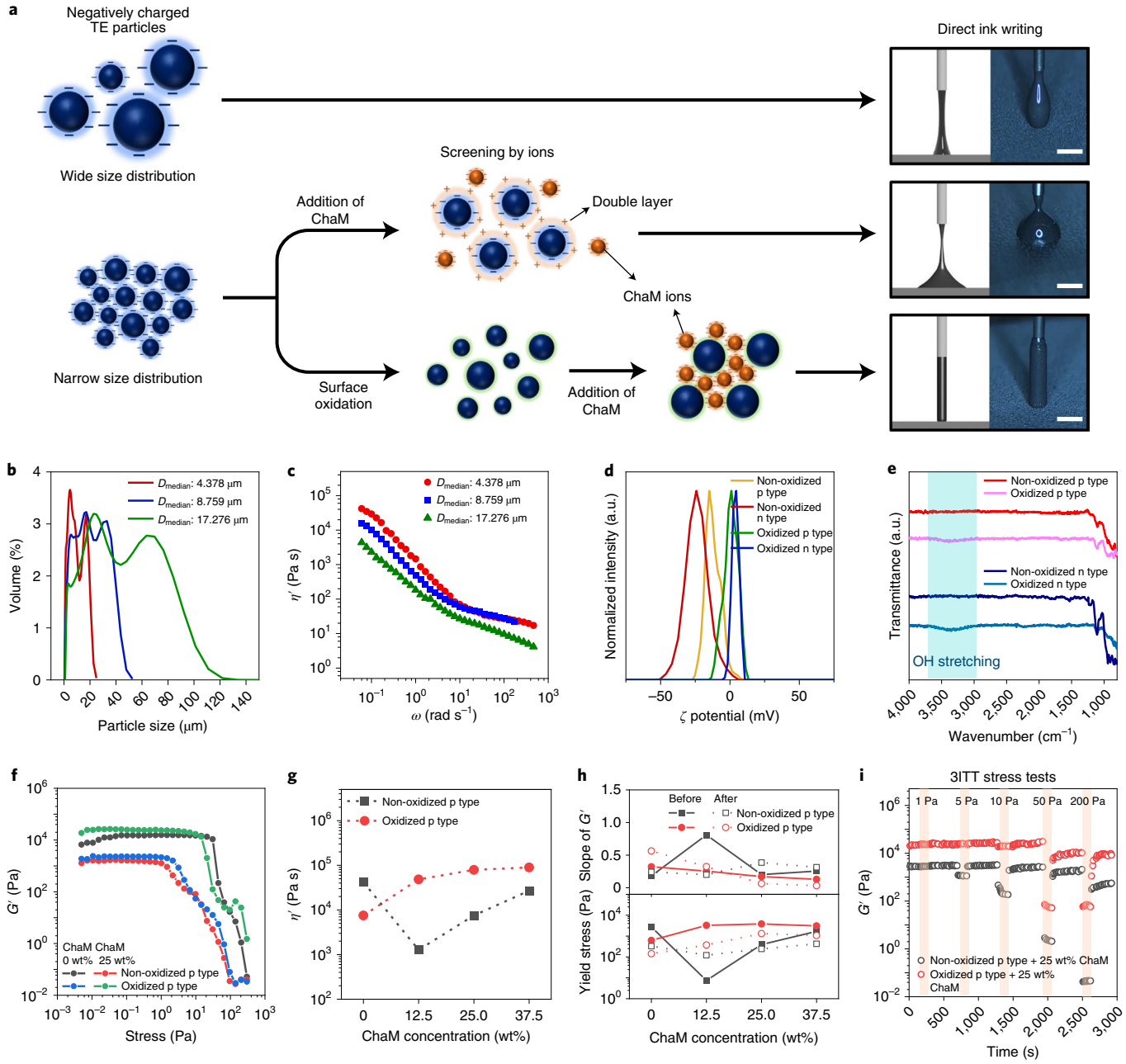

Fig. 2 | Rheological properties of super-viscoelastic TE ink. a, Schematic showing the design principle of super-viscoelastic TE particle inks with respect to their size, size distribution and surface oxidation. Scale bars, 500 μm. **b**,**c**, Particle size (**b**) and dynamic viscosity (η') (**c**) of p-type $Bi_{0.55}Sb_{1.45}Te_3$ TE particle inks. D_{median} denotes the median particle diameter. **d**,**e**, The ζ potential curves (**d**) and FTIR spectra (**e**) of oxidized and non-oxidized p- and n-type TE particles in colloids. **f**, Storage modulus (G') curves of oxidized and non-oxidized p-type TE particle inks containing 0 and 25 wt% ChaM obtained from the stress sweep test. **g**,**h**, The dynamic viscosity (η') values in the static state at 0.1 rad s^{-1} (**g**) and slope of the G' curve (top) and yield stress (bottom) before and after the stress sweep test (**h**). **i**, G' of oxidized and non-oxidized p-type TE inks with 25 wt% ChaM in the sequential 3ITT measurement. In repeated second intervals (vertically shaded lines) where high shear stress is applied, the stress was gradually increased from 1 Pa to 200 Pa.

ink based on the non-oxidized TE particle, suggesting strong inter-particle interaction. These results confirmed that surface oxidation coupled with ChaM substantially improved the 3D printability by attaining both shear thinning and fast elastic recovery—which are rarely demonstrated for extremely high viscous fluids, especially for those without organic binders. This combination of viscoelastic properties is expected to realize binder-free, all-inorganic inks for a precise direct writing process. Supplementary Table 1 lists the most recent development of TE materials and modules based on various 3D printing technologies. To the best of our knowledge, most of the studies involved polymeric binders to improve the viscoelastic behaviour of the ink and the resulting 3D-printed TE module possessed a simple, substrate-assisted shape. However, the current study provides a fundamental route to construct complex 3D TE architectures and μTEMs with a high resolution by tailoring the rheological properties of the ink.

TE properties of direct-written 3D structures

Sinterability observed in direct-written TE filaments was clearly reflected in their high TE properties. All the samples were sintered

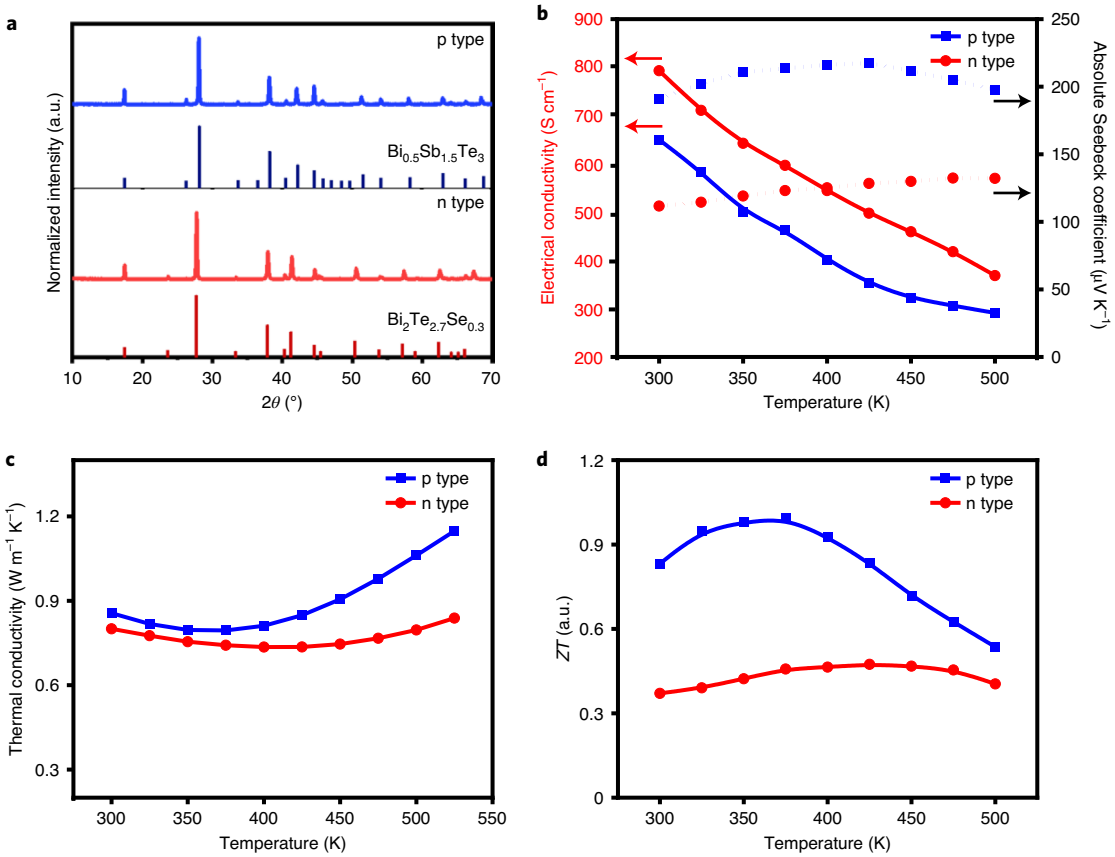

Fig. 3 | TE properties of the 3D-printed samples. a, XRD patterns of 3D-printed n-type and p-type filaments. The vertical lines indicate the peaks corresponding to bulk $Bi_{0.5}Sb_{1.5}Te_3$ (JCPDS: 00-049-1713) and $Bi_2Te_{2.7}Se_{0.3}$ (JCPDS: 00-015-0863). **b**–**d**, Temperature-dependent TE properties of n-type and p-type 3D-printed filaments: electrical conductivities and absolute Seebeck coefficients (**b**), thermal conductivities (**c**) and *ZT* values (**d**).

at 450 °C under H_2 atmosphere to remove the surface oxide layers (Supplementary Fig. 12). The XRD spectra of both p- and n-type particles showed patterns corresponding to bulk $Bi_{0.5}Sb_{1.5}Te_3$ and $Bi_2Te_{2.7}Se_{0.3}$ with slight peak shifts, indicating the effective sintering of materials into a single phase (Fig. 3a). We varied the ChaM content for both p-type $Bi_{0.55}Sb_{1.45}Te_3$ and n-type $Bi_2Te_{2.7}Se_{0.3}$ particles, and the highest figure-of-merit (*ZT*) values were observed for 25 and 10 wt% ChaM content for p- and n-type particles, respectively (Supplementary Fig. 13). Accordingly, the characterizations and related discussion were described for the corresponding samples.

The temperature dependence of TE properties at 300–500 K was characterized using the direct-written filaments with diameters of 300–350 μm. The electrical conductivities of p- and n-type filaments decreased with increasing temperatures, indicating the degenerate behaviour of semiconductors. The Seebeck coefficients of both the samples generally increased with increasing temperatures. The Seebeck coefficient of the p-type filament was 191.2 μV K^{-1} at room temperature with a peak value of 217.5 μV K^{-1} at 425 K, whereas that of the n-type filament ranged within 111.7–132.4 μV K^{-1} over the entire measured temperature range (Fig. 3b). The p- and n-type samples had carrier mobilities of 197.6 and 81.7 cm^2 V^{-1} s^{-1}, respectively, characterized by the Hall effect measurement. These high carrier mobilities are comparable to the reported values of $(Bi,Sb)_2(Te,Se)_3$-based bulk alloys with the corresponding compositions and are responsible for the high electrical conductivity of the 3D-printed samples[33,42]. The carrier concentrations of the p- and n-type samples were 2.1 and 6.3×10^{19} cm^{-3}, respectively. Since the Seebeck coefficient is reciprocally proportional to the carrier concentration, the relatively low Seebeck coefficient of the n-type sample compared with the corresponding bulk values is attributed to the high carrier concentration[33]. Thus, the p- and n-type samples had high TE power factors of 2.4 and 1.0 mW m^{-1} K^{-2}, respectively, at 300 K (Supplementary Fig. 14).

We further compared the electrical properties of direct-written TE filaments with those of 3D-printed p- and n-type TE bulk cuboids that were 12.7 mm wide and 1.0–2.0 mm thick in the corresponding temperature ranges. It was found that their electrical conductivities and Seebeck coefficients were identical to those of the TE filaments within the measurement error range (5–7%). Thus, the homogeneous TE properties of the 3D-printed samples were independent of their dimensions, which demonstrated the expansibility of the current process to materials ranging from micrometre-scale single filaments to centimetre-scale 3D bulks obtained by fusing the deposited TE filaments in a layer-by-layer manner without the loss of TE performance (Supplementary Fig. 15).

Moreover, this homogeneity in the properties allowed us to evaluate the overall TE properties of the direct-written filaments by measuring the thermal properties of the 3D-printed TE bulk cuboids due to the difficulty involved in measuring a microscale single filament. The temperature-dependent thermal conductivity of the p- and n-type bulk cuboids ranged within 0.74–1.15 W m^{-1} K^{-1} over the entire measured temperature range (Fig. 3c), which was considerably reduced in comparison to bulk Bi_2Te_3-based materials (1.5–2.5 W m^{-1} K^{-1}) (ref. [42]). This reduction in thermal conductivities is attributed to phonon scattering at the pore sites of the printed TE materials, which had relative densities of 82% and 72% for the p- and n-type samples, respectively. Because the as-printed samples were sintered under pressure-less conditions

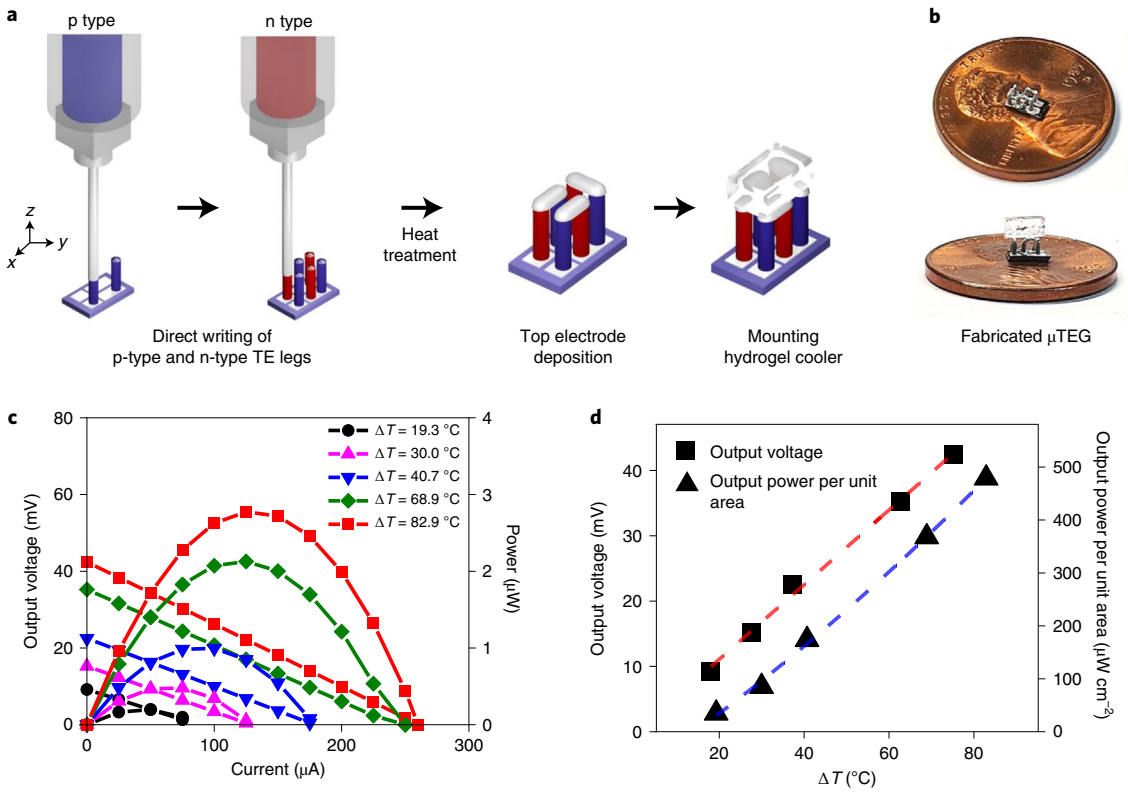

Fig. 4 | Fabrication and power performance of the μTEG. a, Schematic showing the fabrication of the μTEG by direct 3D ink writing. **b**, Photographs of the fabricated μTEG. **c**, Output voltage and power of the μTEG at various temperature differences (ΔT). **d**, Output voltage and power density of the μTEG as a function of temperature difference. The red dashed line was fitted to the data points by a linear fit (voltage ~ ΔT) and the blue dashed line by a second-order polynomial fit (power ~ ΔT^2).

without precompaction, 20–30% porosity was unavoidable. The porosities of the 3D-printed samples are shown in Supplementary Fig. 16. These macroscale pores are beneficial for enhancing the ZT values by the reduction in thermal conductivity. For example, it has been theoretically predicted that an increase in the ratio of electrical conductivity to thermal conductivity of 30% occurs in porous SiGe alloys[43]. In addition, there have been several reported instances showing experimental evidence for the enhancement in ZT values of porous TE materials[44–47]. The thermal properties of 3D-printed samples are shown in Supplementary Fig. 17.

The promising electrical and thermal properties led to markedly high ZT values for the p- and n-type samples. The p- and n-type 3D-printed samples had ZT values of 0.84 and 0.37, respectively, at room temperature (Fig. 3d). Furthermore, the maximum ZT values of 1.0 and 0.5 were achieved at 375 and 425 K for the p- and n-type TE materials, respectively. These values are comparable to those obtained for typical Bi_2Te_3 and BiSbTe ingots ($ZT \approx 0.8$–1.0) (ref. [48]), and higher than the reported value of 0.9 for 3D-printed BiSbTe materials[28]. To the best of our knowledge, the ZT values reported in this paper are one of the highest for TE materials obtained by 3D printing processes (Supplementary Table 1). We further investigated the thermal stability of the 3D-printed samples by the characterization of TE properties under three heat cycles. In these cycles, the electrical conductivities, Seebeck coefficients and thermal conductivities of both p- and n-type samples (Supplementary Fig. 18) were well preserved without any degradation, clearly demonstrating the thermal stability of our samples.

Fabrication and power measurement of μTEG

When combined with traditional patterning processes, our ink writing technique can facilitate the heterogeneous integration of TE legs into patterned electrode arrays, thereby making it possible to fabricate μTEGs in a rapid, direct and cost-effective manner. Moreover, the shape engineerability of the current process makes it possible to design TE legs for optimized thermal transfer, maximizing the temperature gradient and the resulting output power of μTEGs. We fabricated a μTEG composed of 3D-printed vertical TE filaments with a diameter of 350 μm and a height of 1,400 μm. The thickness of the TE leg of the fabricated μTEG is at least an order of magnitude greater than that of previously reported μTEGs prepared by traditional MEMS, hot-pressing and dicing, and screen-printing processes[1,6,10,49,50]. Moreover, p- and n-type TE legs were directly printed on a Si/SiO_2 substrate using prepatterned Ag electrodes (width, 500 μm), which were fabricated by screen printing with a shadow mask (Fig. 4a,b and Supplementary Video 3). The printed TE legs were electrically connected using Ag adhesive. The top of the module was further covered with a water-captured hydrogel cooler for maintaining a temperature difference between the hot and cold sides. Polyacrylamide hydrogel—with a high amount of strongly bound water within the polymeric matrix—prevented premature water evaporation and allowed the sustained maintenance of water-cooling capability for a wide range of temperatures. Under temperature differences from 50 to 80 K, the lifetime of the hydrogel slowly decreased from 330 to 270 s. Beyond this time, the hydrogel completely dehydrated, turning the clear hydrogel opaque. However, before dehydration, under a constant supply of water, the hydrogel maintained the cooling capacity for a long period of time, allowing us to measure the power performance of the μTEG at a steady state. Furthermore, we compared the temperatures of the hot and cold sides of the μTEG with hydrogel and typical thermally conductive pad coolers and without the cooler under heating. As shown in Supplementary Fig. 19b, the μTEG with hydrogel shows the best

cooling performance compared with others, in which the lowest cold-side temperatures and the largest temperature differences were observed over the entire measurement range.

The module resistance was 92 Ω at room temperature. On heating, the hot-side temperature gradually increased from room temperature to 121.8 °C, whereas the cold-side temperature remained at less than 48 °C (Supplementary Fig. 20). Accordingly, the temperature difference across the μTEG increased up to 82.9 °C, which is an order of magnitude higher than the typical temperature gradient observed in previously reported μTEGs on heating[6,11,50]. The creation of such a high temperature difference in the current system is attributed to the high aspect ratio of the 3D-printed TE legs. As the temperature difference increased, the output voltage increased almost linearly and the output power increased quadratically (Fig. 4c,d), achieving a maximum output voltage of 42.4 mV and power of 2.8 μW at a temperature difference of 82.9 °C. Moreover, the maximum power density reached 479.0 μW cm^{-2}, which is sufficient to run advanced wireless sensor networks[3–5,7,51]. Moreover, the output voltage and power were >50% and >100% higher than those of μTEGs without a hydrogel cooler (Supplementary Fig. 19c,d), showing the effectiveness of the hydrogel as a cooling unit in the current μTEG system.

As summarized in Supplementary Table 2, we compared the properties of the current μTEGs with the reported values in printed μTEGs. In every aspect of the materials' properties—aspect ratios of legs and temperature differences—that determine the power-generating performances of μTEGs, our μTEG shows superior values to those reported. Accordingly, a maximum power density of 479.0 μW cm^{-2} observed in our μTEG is at least an order of magnitude higher than the reported values. These results demonstrate the practicability of 3D direct writing for manufacturing high-performance μTEGs that can be integrated into electronic systems.

Conclusions

By optimizing the particle size, size distribution and surface states, we have developed all-inorganic TE inks that have high viscoelasticity and are suitable for the direct 3D writing of TE filaments. A μTEG fabricated using our 3D-printed TE legs exhibited a maximum output voltage of 42.4 mV and power of 2.8 μW at a temperature difference of 82.9 °C, and a maximum power density of 479.0 μW cm^{-2}. Our design strategy can be extended to other classes of functional materials to synthesize 3D-printable inks without using organic rheological modifiers. Such an approach could avoid the loss of the primary properties of particles in 3D-printed structures and help achieve a broader adoption of 3D-printable materials in electronic device manufacturing. Furthermore, by combining the direct writing approach with traditional lithographic processes, it could enable the integration of μTEMs into various emerging electronic systems, where the modules function as power generators for energy-autonomous systems or as Peltier coolers for heat management.

Methods

Materials. Granules of Bi, Sb, Te and Se (99.999%) were purchased from 5N Plus. Ethanethiol (>97%), ethylenediamine (>99.5%), acetonitrile (>99.8%) and glycerol (>99.5%) were purchased from Aldrich. All the elements and chemicals were used without further purification.

Synthesis of $(Bi,Sb)_2(Te,Se)_3$-based TE particles. TE powders with the stoichiometric composition of $Bi_{0.55}Sb_{1.45}Te_3$ and $Bi_2Te_{2.7}Se_{0.3}$ were prepared by mechanical alloying. For the synthesis of $Bi_{0.55}Sb_{1.45}Te_3$ particles with D_{median} of 4.378 μm, zirconia grinding balls with a diameter of 5 mm were loaded in an 80 ml zirconia milling jar and the ball-to-powder weight ratio was fixed at 5:1 (Fritsch Mono Mill, PULVERISETTE). The rotation speed of the planetary mill was 450 r.p.m. and the time of alloying was 11 h. The particles with D_{median} of 17.276 μm were synthesized under the same conditions in a 240 ml zirconia milling jar. The particles with D_{median} of 8.759 μm were synthesized by mechanical alloying using a SPEX mill (8000M mixer/mill, SPEX) with stainless steel balls including two balls (diameter φ = 12.7 mm) and four balls (φ = 6.35 mm) for 5 h. In all the samples, agglomerated particles were removed by sieving the particles to <45 μm.

Synthesis of all-inorganic $(Bi,Sb)_2(Te,Se)_3$-based ink. The Sb_2Te_4 ChaM was synthesized by dissolving 0.32 g Sb powder and 0.64 g Te powder in a co-solvent of 2 ml ethanethiol and 8 ml ethylenediamine at room temperature in a N_2-filled glove box. The Sb_2Te_4 solution was stirred for over 24 h until the particles fully dissolved to produce a dark purple colour. Acetonitrile antisolvent was added to the solution with the volume ratio of 8:1, which is followed by centrifugation at 6,615 g for 10 min to precipitate out the precursor. The precipitate was dried under a vacuum for 30 min to produce Sb_2Te_4 ChaM powder. A mixture of 4 g TE powder and the desired amount of ChaM was dispersed in 4 g glycerol, and the solution was mixed with a planetary centrifugal mixer (ARM-100, Thinky) for 2 h to fully homogenize the ink.

Rheological properties of the ink. The rheological properties of TE inks were measured using a rotational rheometer (HAAKE MARS III, Thermo Scientific) equipped with a coaxial cylinder geometry at 25 °C. The stress sweep tests were conducted over the range of 0.005–300 Pa at a frequency of 1 rad s^{-1} and the frequency sweep tests were carried out before and after the stress sweep test at a constant stress of 1 Pa to assess the phase stability of the ink. The 3ITTs at various stresses were also conducted as reported elsewhere[40]. The first interval was conducted under a constant shear stress of 0.1 Pa (linear viscoelastic range) for 120 s. The second interval was done at various stresses (1, 5, 10, 50 and 200 Pa) for 120 s. The third interval was attempted at a shear stress of 0.1 Pa for 300 s to evaluate the structural recovery of the ink after deposition during 3D printing.

Direct 3D writing process. Direct writing was executed using an in-house pneumatic extrusion-based 3D printer with a nozzle connected to an ink reservoir, a pressure controller, a compressor unit and a three-axis stage with a stepper motor. Ink was loaded in a 5 ml syringe barrel (Saejong) with a metal needle having inner diameters ranging from 80 to 310 μm and deposited along the z axis at 0.25 mm s^{-1}. The pressure control unit was adjusted to extrude a filament at a high aspect ratio.

Material characterization. XRD patterns were collected by using X'pert Pro (PANalytical) with a Cu Kα X-ray source (wavelength, 1.5418 nm), operating at 40 kV and 30 mA equipped with an X'Celerator detector. The microstructure was characterized by using a field-effect SEM (FEI Nova NanoSEM 230 and S-4800 (Hitachi High-Tech)) operated at 10 kV. The OM images were obtained using an Olympus BX51M instrument. The CCD images were obtained by a CCD camera (MicroPublisher 5.0 RTV, QImaging). Particle size distributions of the TE powders were determined with a laser particle size analyser (LS 13 320, Beckman Coulter). The ζ potential of the particles was determined by a Zetasizer Nano ZS instrument (Malvern). The surface functional groups of the particles were obtained using an FTIR spectrometer (Varian 670/620) in the attenuated total reflectance mode over the scanning range of 650–4,000 cm^{-1}. The XPS measurements were performed by an X-ray photoelectron spectrometer (K-Alpha, Thermo Scientific).

TE properties of 3D-printed samples. The electrical conductivity of the filaments was measured using the sheet resistance of the samples by a four-point method (Keithley 2400 multimeter controlled with LabTracer 2.0 software, Keithley Instruments). The Seebeck coefficient was obtained by using a home-built setup in which the temperature gradient and open-circuit voltage were measured using a Keithley 2400 sourcemeter. The Seebeck coefficient was calculated by the slope of the measured voltages versus the applied temperature differences ranging from 1 to 5 K, which was measured by two T-type thermocouples. For the temperature-dependent properties, the measuring setup was placed on a hot plate and the measuring temperatures were controlled by heating two ceramic heaters.

The temperature-dependent electrical conductivity and Seebeck coefficients of the bulk materials were simultaneously measured under an Ar atmosphere in the temperature range from 300 to 500 K using a thermal analyser (SBA 458 Nemesis, NETZSCH). A typical sample for measurement had a cuboid shape with dimensions 10 × 10 × 2 mm^3. The thermal conductivity (κ) was calculated from the relationship $\kappa = \rho C_p D$, where ρ is the density, C_p is the specific heat capacity and D is the thermal diffusivity. The thermal diffusivity was measured in the temperature range of 300–500 K by using a laser flash analyser (LFA-457, NETZSCH). The specific heat capacity was determined using the rule of mixtures with the previously reported specific heat capacity values of Bi_2Te_3 and Sb_2Te_3 (refs. [52,53]). The density was estimated by measuring the volume and weight of the cuboid shape. The carrier concentrations and mobilities were measured at room temperature by using a Hall measurement system (HMS-8400, Lake Shore) with a magnetic field of ±10 T.

Fabrication and output power characterization of the μTEG. Ag electrodes were screen-printed on a SiO_2 wafer using Ag-containing adhesive (Pyro-Duct 597-A, Aremco), as illustrated in Supplementary Fig. 21. On top of the Ag electrodes, three pairs of n- and p-type TE filaments were extruded out of a metal needle with an inner diameter of 210 μm. The printed filaments were initially dried at 110 °C on a hot plate for 5 min and annealed at 450 °C for 30 min in a tube furnace by flowing

a gas mixture of 15% H_2 and 85% Ar. Each pair of TE filaments was electrically connected in series and thermally in parallel by bridging the Ag-containing adhesive on top of the annealed filaments. To measure the temperature difference across each pair of TE filaments, two T-type thermocouples were attached to the surface of the SiO_2 wafer (hot side) and on top of the Ag electrodes (cold side). The ceramic heater ($10 \times 10\,mm^2$) was used as a heat source and the cold-side temperature was maintained below 48 °C by attaching polyacrylamide hydrogel or thermally conductive pad (Thermally Conductive Silicone Interface Pad 5591, 3M) on top of the μTEG. The polyacrylamide hydrogel was separately fabricated by the radical polymerization of 10% (w/v) acrylamide and 0.5% (w/v) *N*,*N*′-methylenebisacrylamide, with 0.2% (w/v) ammonium persulfate and 0.2% (w/v) *N*,*N*,*N*′,*N*′-tetramethylethylenediamine as the co-initiators[54]. For the measurement of power generation, the TEG was connected to a Keithley 2400 instrument at each temperature difference and the maximum power output (P) was calculated using $P = V^2/4R$, where V is the voltage and R is the resistance. Thermal silicone grease (YYTG-201, Youngyiel) was applied between the heater and μTEG to minimize the thermal contact resistance.

Data availability

The data that support the findings of this study are available from the corresponding authors upon reasonable request.

Received: 13 January 2021; Accepted: 5 July 2021;
Published online: 9 August 2021

References

1. Haras, M. & Skotnicki, T. Thermoelectricity for IoT—A review. *Nano Energy* **54**, 461–476 (2018).
2. Ando, J. et al. A review of the development and applications of thermoelectric microgenerators for energy harvesting. *Renew. Sustain. Energy Rev.* **91**, 376–393 (2018).
3. Pletcher, N. M. et al. A 52 μW wake-up receiver with −72 dBm sensitivity using an uncertain-IF architecture. *IEEE J. Solid-State Circuits* **44**, 269–280 (2009).
4. Gilbert, J. M. & Balouchi, F. Comparison of energy harvesting systems for wireless sensor networks. *Inter. J. Autom. Comput.* **5**, 334–347 (2008).
5. Zhang, Y. et al. A batteryless 19 μW MICS/ISM-band energy harvesting body sensor node SoC for ExG applications. *IEEE J. Solid-State Circuits* **48**, 199–213 (2013).
6. Yan, J. et al. Review of micro thermoelectric generator. *J. Microelectromech. Syst.* **27**, 1–18 (2018).
7. Rabaey, J. M. et al. PicoRadios for wireless sensor networks: the next challenge in ultra-low power design. In *2002 IEEE ISSCC Digest of Technical Papers*, 200–201 (2002).
8. Park, S. C. et al. A micro-thermoelectric gas sensor for detection of hydrogen and atomic oxygen. *Analyst* **134**, 236–242 (2009).
9. Blachowicz, T. & Ehrmann, A. 3D printed MEMS technology—recent developments and applications. *Micromachines* **11**, 434 (2020).
10. Dhawan, R. et al. $Si_{0.97}Ge_{0.03}$ microelectronic thermoelectric generators with high power and voltage densities. *Nat. Commun.* **11**, 4362 (2020).
11. Li, G. et al. Integrated microthermoelectric coolers with rapid response time and high device reliability. *Nat. Electron.* **1**, 555–561 (2018).
12. Hong, C. T. et al. Spray-printed CNT/P3HT organic thermoelectric films and power generators. *J. Mater. Chem. A* **3**, 21428–21433 (2015).
13. Wang, Y. et al. Flexible thermoelectric materials and generators: challenges and innovations. *Adv. Mater.* **31**, 29 (2019).
14. Mehran, M. & Zorman, C. A. SiC MEMS: opportunities and challenges for applications in harsh environments. *Thin Solid Films* **355–356**, 518–524 (1999).
15. Davidson, E. C. et al. 3D printable and reconfigurable liquid crystal elastomers with light-induced shape memory via dynamic bond exchange. *Adv. Mater.* **32**, 1 (2020).
16. Hensleigh, R. et al. Charge-programmed three-dimensional printing for multi-material electronic devices. *Nat. Electron.* **3**, 216–224 (2020).
17. Vyatskikh, A. et al. Additive manufacturing of 3D nano-architected metals. *Nat. Commun.* **9**, 593 (2018).
18. Lewis, J. A. & Ahn, B. Y. Device fabrication: three-dimensional printed electronics. *Nature* **518**, 42–43 (2015).
19. Sun, K. et al. 3D printing of interdigitated Li-ion microbattery architectures. *Adv. Mater.* **25**, 4539–4543 (2013).
20. Lewis, J. A. Direct ink writing of 3D functional materials. *Adv. Funct. Mater.* **16**, 2193–2204 (2006).
21. Jo, S. et al. Ink processing for thermoelectric materials and power-generating devices. *Adv. Mater.* **31**, 1804930 (2019).
22. Zhang, B. et al. Promising thermoelectric properties of commercial PEDOT:PSS materials and their Bi_2Te_3 powder composites. *ACS Appl. Mater. Interfaces* **2**, 3170–3178 (2010).
23. Kato, K. et al. Fabrication of bismuth telluride thermoelectric films containing conductive polymers using a printing method. *J. Electron. Mater.* **42**, 1313–1318 (2013).
24. Ou, C. et al. Fully printed organic–inorganic nanocomposites for flexible thermoelectric applications. *ACS Appl. Mater. Interfaces* **10**, 19580–19587 (2018).
25. He, M. et al. Thermopower enhancement in conducting polymer nanocomposites via carrier energy scattering at the organic–inorganic semiconductor interface. *Energy Environ. Sci.* **5**, 8351–8358 (2012).
26. Burton, M. R. et al. 3D printed SnSe thermoelectric generators with high figure of merit. *Adv. Energy Mater.* **9**, 1900201 (2019).
27. Su, N. et al. 3D-printing of shape-controllable thermoelectric devices with enhanced output performance. *Energy* **195**, 116892 (2020).
28. Kim, F. et al. 3D printing of shape-conformable thermoelectric materials using all-inorganic Bi_2Te_3-based inks. *Nat. Energy* **3**, 301–309 (2018).
29. Yang, S. E. et al. Composition-segmented BiSbTe thermoelectric generator fabricated by multimaterial 3D printing. *Nano Energy* **81**, 105638 (2021).
30. Kim, S. I. et al. Dense dislocation arrays embedded in grain boundaries for high-performance bulk thermoelectrics. *Science* **348**, 109–114 (2015).
31. Li, J.-F. et al. High-performance nanostructured thermoelectric materials. *NPG Asia Mater.* **2**, 152–158 (2010).
32. Saeidi-Javash, M. et al. 3D conformal printing and photonic sintering of high-performance flexible thermoelectric films using 2D nanoplates. *Adv. Funct. Mater.* **29**, (2019).
33. Snyder, G. J. & Toberer, E. S. Complex thermoelectric materials. *Nat. Mater.* **7**, 105–114 (2008).
34. Bark, H. et al. Effect of multiwalled carbon nanotubes on the thermoelectric properties of a bismuth telluride matrix. *Curr. Appl. Phys.* **13**, S111–S114 (2013).
35. Willenbacher, N. & Georgieva, K. in *Product Design and Engineering: Formulation of Gels and Pastes* (eds Bröckel, U et al.) Ch. 1, 7–49 (Wiley, 2013).
36. Barthelmes, G. et al. Particle size distributions and viscosity of suspensions undergoing shear-induced coagulation and fragmentation. *Chem. Eng. Sci.* **58**, 2893–2902 (2003).
37. Luckham, P. F. & Ukeje, M. A. Effect of particle size distribution on the rheology of dispersed systems. *J. Colloid Interface Sci.* **220**, 347–356 (1999).
38. Chen, Z. et al. Preparation of high solid loading and low viscosity ceramic slurries for photopolymerization-based 3D printing. *Ceram. Int.* **45**, 11549–11557 (2019).
39. Maranzano, B. J. & Wagner, N. J. The effects of interparticle interactions and particle size on reversible shear thickening: hard-sphere colloidal dispersions. *J. Rheol.* **45**, 1205–1222 (2001).
40. Eom, Y. et al. Rheological design of 3D printable all-inorganic inks using BiSbTe-based thermoelectric materials. *J. Rheol.* **63**, 291–304 (2019).
41. Hong, B. J. et al. Successful stabilization of graphene oxide in electrolyte solutions: enhancement of biofunctionalization and cellular uptake. *ACS Nano* **6**, 63–73 (2012).
42. Zheng, G. et al. High thermoelectric performance of p-BiSbTe compounds prepared by ultra-fast thermally induced reaction. *Energy Environ. Sci.* **10**, 2638–2652 (2017).
43. Lidorenko, N. S. et al. Influence of porosity and intergrain-boundary quality on the electrical and thermal conductivities of semiconductive thermoelectric materials. *Inorg. Mater.* **6**, 1853 (1970).
44. Wu, C.-A. et al. Low thermal conductivity and enhanced zT values of porous and nanostructured $Cu_{1-x}Ni_x$ alloys. *Chem. Eng. J.* **368**, 409–416 (2019).
45. Khan, A. U. et al. Nano-micro-porous skutterudites with 100% enhancement in ZT for high performance thermoelectricity. *Nano Energy* **31**, 152–159 (2017).
46. Chang, P. H. et al. Giant thermoelectric effect in graphene-based topological insulators with heavy adatoms and nanopores. *Nano Lett.* **14**, 3779–3784 (2014).
47. Ning, H. et al. Enhanced thermoelectric performance of porous magnesium tin silicide prepared using pressure-less spark plasma sintering. *J. Mater. Chem. A* **3**, 17426–17432 (2015).
48. Yan, X. et al. Experimental studies on anisotropic thermoelectric properties and structures of n-type $Bi_2Te_{2.7}Se_{0.3}$. *Nano Lett.* **10**, 3373–3378 (2010).
49. Rojas, J. P. et al. Review—Micro and nano-engineering enabled new generation of thermoelectric generator devices and applications. *ECS J. Solid State Sci. Technol.* **6**, N3036–N3044 (2017).
50. Francioso, L. et al. Flexible thermoelectric generator for ambient assisted living wearable biometric sensors. *J. Power Sources* **196**, 3239–3243 (2011).
51. Paradiso, J. A. & Starner, T. Energy scavenging for mobile and wireless electronics. *IEEE Pervasive Comput.* **4**, 18–27 (2005).
52. Pashinkin, A. S. et al. The heat capacity of solid antimony telluride Sb_2Te_3. *Russ. J. Phys. Chem.* **82**, 878–879 (2008).
53. Liu, W. et al. Studies on the Bi_2Te_3–Bi_2Se_3–Bi_2S_3 system for mid-temperature thermoelectric energy conversion. *Energy Environ. Sci.* **6**, 552–560 (2013).

54. Kim, M. & Cha, C. Modulation of functional pendant chains within poly(ethylene glycol) hydrogels for refined control of protein release. *Sci. Rep.* **8**, 4315 (2018).

Acknowledgements
This work was supported by the Samsung Research Funding Center of Samsung Electronics under project no. SRFC-MA1801–05. J.S.S. acknowledges the Nano-Material Technology Development Program (NRF-2018M3A7B8060697) and the Creative Materials Discovery Program (NRF-2020M3D1A1110502) through the National Research Foundation (NRF) funded by the Ministry of Science and ICT, Republic of Korea.

Author contributions
F.K., S.E.Y., H.J., H.G.C. and J.S.S. designed the experiments, analysed the data and wrote the paper. F.K., S.E.Y., S.C., J.L., J.S.S. and K.T.K. carried out the synthesis and basic characterization of the materials. S.E.Y., H.J. and H.G.C. performed the characterization of rheological properties. F.K., S.E.Y., G.K. and S.A. performed the characterization of thermoelectric properties. F.K. and S.E.Y. carried out the fabrication and measurement of TEGs. S.K. and C.C. performed the synthesis of hydrogels. All the authors discussed the results and commented on the manuscript.

Competing interests
The authors declare no competing interests.

Additional information
Supplementary information The online version contains supplementary material available at https://doi.org/10.1038/s41928-021-00622-9.

Correspondence and requests for materials should be addressed to H.G.C. or J.S.S.

Peer review information *Nature Electronics* thanks Yanzhong Pei, Kyu Huong Lee and the other, anonymous, reviewer(s) for their contribution to the peer review of this work.

Reprints and permissions information is available at www.nature.com/reprints.

Publisher's note Springer Nature remains neutral with regard to jurisdictional claims in published maps and institutional affiliations.

© The Author(s), under exclusive licence to Springer Nature Limited 2021